Nanoscale

PAPER

View Article Online
View Journal

Cite this: DOI: 10.1039/d5nr04000k

Multi-peak single object emission of $MAPbBr_3$ nanoplatelets synthesised using a non-template ligand-assisted reprecipitation route

Suhaas Gupta, *[a] Dmytro Vorontsov,[b] Anna Fučíková,[b] František Trojánek,[b] Dominika Zákutná, [c,d] Jozef Veselý, [e] Petr Harcuba[e] and Milan Dopita [a]

We report a modified non-template ligand-assisted reprecipitation synthesis of colloidal methylammonium lead bromide ($MAPbBr_3$) perovskite nanoplatelets (NPLs). The room-temperature process yields highly monodisperse, square-shaped NPLs that are stabilised by oleic acid and *n*-octylammonium bromide surface ligands. Scanning transmission electron microscopy (STEM) confirms the ultrathin square-shaped morphology of the synthesised NPLs with lateral dimensions of 17–20 nm. X-ray diffraction (XRD) reveals a cubic perovskite phase ($Pm\bar{3}m$) with a strong (100) orientation, and MicroStructure fitting reveals the contribution from two crystallite sizes of 18.3 nm and 117.9 nm. Small-angle X-ray scattering (SAXS) data, when fitted using a Guinier–Porod function, confirms the quasi-2D confinement of the NPLs, supporting the morphology observed in STEM analysis. Further fitting using a lamellar model reveals a thickness of 13.5 nm. Ensemble optical spectroscopy exhibits a sharp photoluminescence emission (PLE) peak at 518 nm with a narrow peak-width of 26 nm, a quantum yield of ~50%, a single-exponential PL decay time of 11.9 ns, and an optical band-gap of 2.3 eV derived from the Tauc analysis of the UV-Visible absorption spectrum. Single-dot spectroscopy reveals pronounced multi-peak emission behaviour, caused by quantum confinement effects promoted by atmospheric oxygen and laser-assisted photoactivation. This work provides a reproducible route to high-quality $MAPbBr_3$ NPLs, with properties ideal for optoelectronic and quantum photonic applications like perovskite-based LEDs and ultrathin photodetectors.

Received 22nd September 2025,
Accepted 22nd December 2025

DOI: 10.1039/d5nr04000k

rsc.li/nanoscale

1. Introduction

Hybrid organic–inorganic metal halide perovskites, particularly methylammonium lead halide perovskites having the general formula $CH_3NH_3PbX_3$ (where X = Cl, Br, I), have emerged as highly promising materials in the field of optoelectronics and photovoltaics due to their exceptional optical and electronic properties. These materials uniquely combine the structural and thermal stability of inorganics with the solution-processability and tuneable optoelectronic characteristics of organics. Hybrid perovskites in the bulk form are popular photovoltaic materials due to their high charge carrier mobility and long carrier diffusion lengths and lifetimes, while their nano-sized properties include high photoluminescence quantum yields, tuneable band-gaps, narrow emission linewidths, and strong absorption coefficients.[1–4] Such features make perovskite materials especially suitable for applications in solar cells, LEDs, lasers, photodetectors, and X-ray imaging, among others.[5–8] The efficiency of perovskite-based solar cells has soared dramatically in recent years, and perovskite-based LEDs (PeLEDs) have demonstrated external quantum efficiencies (EQEs) exceeding 20% for red and near-infrared emission.[9–11]

Among the family of hybrid perovskites, methylammonium lead bromide ($MAPbBr_3$) has drawn significant attention due to its favourable band-gap (~2.2 eV), high photoluminescence, and low exciton binding energy (~40 meV), which closely matches thermal energy at room temperature. These characteristics enable efficient excitonic transitions under ambient conditions, making $MAPbBr_3$ an attractive material for green-light LEDs, solar cells, and optical sensors. Furthermore, $MAPbBr_3$ exhibits a stable exciton absorption for every phase it crystallises in, making it suitable for temperature-tolerant optoelectronic devices.[12–14] Its nanostructured forms, particularly quantum dots and nanoplatelets, offer enhanced luminescence due to quantum confinement, enabling emission

[a]Department of Condensed Matter Physics, Faculty of Mathematics and Physics, Charles University, Ke Karlovu 5, 12116 Prague 2, Czech Republic. E-mail: suhaas96@gmail.com
[b]Department of Chemical Physics and Optics, Faculty of Mathematics and Physics, Charles University, Ke Karlovu 5, 12116 Prague 2, Czech Republic
[c]Department of Inorganic Chemistry, Faculty of Science, Charles University, Hlavova 2030/8, 12843 Prague 2, Czech Republic
[d]Institut Laue-Langevin – The European Neutron Source, 71 avenue des Martyrs, F-38042 Grenoble, France
[e]Department of Physics of Materials, Faculty of Mathematics and Physics, Charles University, Ke Karlovu 5, 12116 Prague 2, Czech Republic

tuning and higher radiative recombination rates. These features, coupled with its relatively facile synthesis and tuneable optoelectronic properties, position $MAPbBr_3$ as a leading candidate for next-generation display technologies, multijunction solar cells, and low-threshold lasers.[15,16] However, like its all-inorganic counterparts, it still suffers from environmental instability, emphasizing the need for continued development in encapsulation, passivation, and synthetic control to ensure long-term operational durability.[17–20]

Single-dot spectroscopy (SDS) offers a transformative advantage over conventional ensemble measurement techniques by enabling the direct investigation of individual nanoparticles' optical properties, thereby revealing intrinsic heterogeneities that are otherwise masked in bulk measurements. Nanoparticles, even when synthesized in the same batch, exhibit some variability in size, shape, surface chemistry, defect states, and local environment – all of which can significantly affect their optical and electronic properties. While ensemble spectroscopy averages these differences, often diluting or obscuring signals from unique or functionally important subpopulations, SDS isolates and resolves the contributions of individual particles. SDS also enables correlation with structural data from tools like electron microscopy, providing a more complete picture of nanoparticle behaviour. Thus, SDS is indispensable for advancing nanotechnology by offering insight into particle-level structure–function relationships that are crucial for reproducibility, device design, and targeted applications.[21–23] Tachikawa *et al.*[24] observed laser illuminated 4-step single particle photoluminescence activation in spherical $MAPbBr_3$ nanoparticles; Freppon *et al.*[25] observed the single particle luminescence from $CH_3NH_3Pb(Br_{1-x}I_x)_3$ (x = 0, 0.25, 0.5, 0.75, 1) nanocrystals; Kimura *et al.*[26] observed the single particle luminescence activation and deactivation from spherical $CH_3NH_3PbBr_3$ nanoparticles; Jana *et al.*[27] observed the single particle luminescence from $Pb(OH)_2$-coated $MAPbBr_3$ and $MAPbBr_{3-x}Cl_x$ nanotubes; Karimata *et al.*[28] observed the single particle luminescence during the *in situ* halide-exchange transition of $CH_3NH_3Pb(I_{1-x}Br_x)_3$ nanocrystals. Based on the literature survey, the authors of the present work therefore report for the first time on the SDS of $MAPbBr_3$ nanoplatelets (NPLs) synthesised using a wet-chemical route. The SDS results reported in this investigation reveal a novel multi-peak PL emission from single isolated $MAPbBr_3$ NPLs synthesised using a non-template ligand-assisted reprecipitation technique. The present work attempts to fill a gap in the knowledge of the correlation between the structure and optical properties of $MAPbBr_3$ NPLs, by employing SDS among other structural and optical ensemble characterisations.

2. Experimental

2.1. Materials and synthesis

$MAPbBr_3$ NPLs were synthesised using the non-template ligand-assisted reprecipitation method as used by Zhang *et al.*[29] with modifications based on the non-template reverse microemulsion procedure used by Rosa-Pardo *et al.*[30] to simplify the overall process and improve the post-synthesis purification protocol. The non-template ligand-assisted reprecipitation synthesis route performed at room temperature typically has low yields due to the formation of undesirable large particles, while the reverse microemulsion synthesis route is performed at high temperatures using challenging precursor compounds; the synthesis procedure hence described attempts to resolve the issues while retaining the advantages of both procedures. Oleic acid [OLA, $C_{18}H_{34}O_2$ (technical grade, 90%)], *n*-octylammonium bromide [OABr, $CH_3(CH_2)_7NH_3Br$], methylammonium bromide [MABr, CH_3NH_3Br (≥99%, anhydrous)] and lead(II) bromide [$PbBr_2$ (99.999% metals basis)] were used as precursors, while *N*,*N*-dimethylformamide [DMF, C_3H_7NO (≥99%, molecular biology)] and toluene [$C_6H_5CH_3$ (for analysis, GR)] were used as the solvents. The precursors and DMF were obtained from Sigma-Aldrich (Merck), and the toluene was obtained from Lach:Ner; all precursors and solvents were used as obtained without further purification. The precursors were dissolved in 1 mL DMF (polar precursor solvent) in ambient conditions with vigorous stirring to make a final solution having molar concentrations of 0.06 M OLA, 0.02 M OABr, 0.04 M MABr and 0.02 M $PbBr_2$. After 10 minutes of stirring, the mixture was injected rapidly into 17 mL of vigorously stirred toluene (non-polar crashing solvent) under ambient conditions. The solution instantly turns a bright yellow-green, which indicates the precipitation of the required colloidal $MAPbBr_3$ crystals. After another 10 minutes of stirring, the yellow-green dispersion was centrifuged at 4000 rpm for 20 minutes, and the precipitate was redispersed in pure toluene for a second centrifugation round at 2000 rpm to separate the largest particles and agglomerates. The supernatant thus obtained was then allowed to sediment overnight at 2–3 °C, and the final colloidal dispersion of the required $MAPbBr_3$ nanoplatelets was used for all characterisations; the colloidal dispersion of NPLs in toluene was found to be structurally and optically stable in the dark at 2–3 °C for at least 4 months.

Hybrid organic–inorganic lead–halide perovskites take the general stoichiometric form of $APbX_3$, where 'X' represents the halide anion and 'A' represents the organic ammonium cation, which are Br^- and $CH_3NH_3^+$, respectively, in the case of $MAPbBr_3$ perovskites. The structure of these perovskites is in the form of a 6-fold coordination of lead cations, which are surrounded by an octahedron of halide ions, with the methyl ammonium ions being embedded in the voids created by the $PbBr_6^{2-}$ corner-sharing octahedra. However, these voids are not big enough for the longer alkyl chain cations of OLA and OABr, which only fit on the outside of the octahedral structure, thereby acting as capping ligands for the nanostructures. In the synthesis process described above, the OLA and OABr ligands are paramount to restricting the growth of the $MAPbBr_3$ platelets to the nano-scale and to limit crystallisation in out-of-plane directions. The post-synthesis purification protocol is also crucial to obtaining the required $MAPbBr_3$ NPLs.

The initial centrifugation cycle removes any unreacted precursor material, and the second centrifugation cycle separates the largest agglomerates from the colloidal dispersion of NPLs. The final overnight sedimentation ensures that only the smallest NPLs completely surrounded by the long chain alkyl ligands are stably dispersed in the toluene solvent. The long chain alkyl ligands are key to forming a homogenous colloidal dispersion of the NPLs in toluene, as they bind to the undercoordinated Br^- anions on the surface. While toluene is termed as a 'poor solvent' in this synthesis due to the poor solubility of the precursors, it is required to stabilise the colloidal dispersion of the NPLs capped by hydrophobic ligands, since toluene is in fact a good solvent when it concerns the ligands. Free-standing OLA ligands dissolved in the toluene also contribute to the structural confinement of the $MAPbBr_3$ NPLs, replacing any ligands that detach from the surface of the NPLs. Interestingly, when the centrifuged precipitate was dispersed in acetone, it spontaneously assembled into micrometre sized clear rods when left to sediment overnight; the authors plan to conduct an *in situ* investigation on this process and subsequently formed material in due course.

2.2. Characterisations

High-angle annular dark-field scanning transmission electron microscopy (STEM) was performed on a JEOL JEM-2200FS Field Emission Electron Microscope operated at an accelerating voltage of 200 kV. Scanning electron microscopy (SEM) was performed on a Thermo Fisher Scientific Apreo 2 SEM, operated in an immersion mode with beam deceleration, with a landing energy of 2 kV. The SEM was equipped with a middle in-lens detector and an upper in-lens detector. X-ray diffraction (XRD) was performed on a Rigaku SmartLab diffractometer configured in a Bragg–Brentano geometry with a 9 kW copper rotating anode X-ray source (incident beam of Cu-Kα radiation with λ = 0.15418 nm) with a parabolic multilayer mirror in the primary beam. The diffractometer was equipped with a HighPix-3000 2D hybrid pixel single photon counting detector, and a set of axial divergence eliminating soller slits in the incident as well as the diffracted beam with an acceptance of 5°. Small-angle X-ray scattering (SAXS) was performed on a Xenocs Xeuss 2.0 SAXS instrument configured in a transmission geometry equipped with a copper microfocus X-ray source (incident beam of Cu-Kα radiation with λ = 0.15418 nm), with two sets of scatter-less slits and a parallel beam collimating single reflection toroidal mirror in the primary beam. The SAXS instrument was equipped with a Dectris Pilatus 200k detector and the sample-to-detector distance was 2500 mm.

UV-Visible absorption spectroscopy was performed on an Analytik Jena SPECORD 250 double-beam spectrophotometer. Ensemble photoluminescent (PL) spectroscopy was performed on a custom home-made setup based on an inverted microscope (Olympus IX-71) coupled to a 30 cm imaging spectrograph (Action SpectraPro-2300i) with a liquid nitrogen cooled back-illuminated CCD camera (Princeton Instruments Spec-10:400B) in the detection path; the sample was excited with a 405 nm diode laser. The same setup was used to perform the single-dot spectroscopy (SDS) to measure the photoluminescence spectra of individual NPLs at room temperature; an objective lens with high magnification (100×) was employed for the collection of the luminescence response, and the backport excitation of the sample. PL quantum yield (QY) measurements were performed in the integrating sphere (10 cm diameter, SphereOptics GmbH); the PL of the samples was excited by a 473 nm laser, and the emission light was coupled by a fused silica fibre bundle to the detection setup described above. For the time-resolved PL decay measurements the sample was excited by a third harmonic frequency (343 nm) of the femtosecond laser NKT Photonics Origami XP/S (1030 nm, 300 fs, 4 W, 50–1000 kHz); the PL signal was detected by a streak camera Hamamatsu C5680 (operated in a single sweep regime with a time resolution of 100 ps) coupled to spectrograph Acton. Atomic force microscopy (AFM) was performed using a JPK NanoWizard3 AFM equipped with an ACTA cantilever obtained from AppNano and operated in an AC mode (semi-contact mode).

3. Results and discussion

3.1. STEM analysis

For the electron microscopy imaging, the sample was prepared by dropping 0.5 μL of the colloidal dispersion on a Cu/holey-carbon transmission electron microscope (TEM) grid (grid size 400 mesh, average hole diameter 100 nm), and the toluene solvent evaporated within a minute at room temperature. Fig. 1(a) shows the STEM micrograph for the synthesised $MAPbBr_3$ NPLs. It can be observed from the micrograph that the synthesised $MAPbBr_3$ nanostructures are in the form of mostly square-shaped nanoplatelets having an edge size from as small as a few nm to as large as 55 nm, with the largest number of dispersed square-shaped NPLs having an edge size of 10–15 nm, as can be seen in the size-distribution histogram shown in Fig. 1(b). Analysis of the histogram with a normal distribution function gives a mean edge length = 20.88 nm with a standard deviation of 10.56, and a mean edge width = 20.36 nm with a standard deviation of 9.99. Gaussian fitting of the size-distribution histogram gives peak values for NPL edge length = 17.82 ± 2.58 nm and NPL edge width = 17.49 ± 1.96 nm. The micrograph also reveals the high degree of dispersibility of the low-concentration colloidal dispersion as evidenced by the lack of overlapping NPLs which would show up in varying brightness contrasts.

Fig. 1(c) shows the STEM micrograph for the synthesised $MAPbBr_3$ NPLs at a higher magnification and reveals the previously documented instability of $MAPbBr_3$ under an electron beam. Even during the process of a single acquisition, the NPLs very quickly 'melt' into an array of much smaller spherical particles, much quicker than previously reported instances of similar observations.[31–33] While the exact composition of these dot-like nanoparticles raises questions in a number of different reports, Sichert *et al.*[34] reported that the degradation of $MAPbBr_3$ under an electron beam formed such quasi-

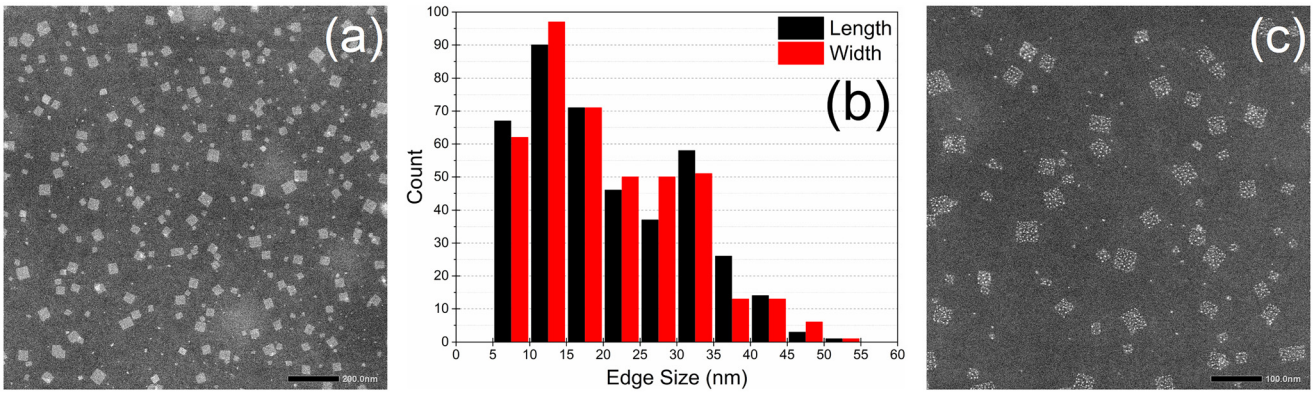

Fig. 1 (a) STEM image of the synthesised $MAPbBr_3$ NPLs; (b) particle size distribution histogram obtained from STEM image in (a); (c) STEM image of the synthesised $MAPbBr_3$ NPLs at higher magnification showing the 'melting' of the nanoplatelets.

spherical crystalline nanoparticles with distances and angles of lattice planes closely matching those characteristic of metallic lead, and showed with energy dispersive X-ray (EDX) spectroscopy that these nano-sized dots did in fact contain metallic lead alongside bromine. With respect to our STEM analysis, the rapid degradation of the synthesised $MAPbBr_3$ NPLs reveals the extremely thin nature of the dispersed NPLs, but unfortunately also presents a hard upper limit of maximum magnification (×100k in our case), limiting the scope of employing electron micrography to determine the exact microstructure and/or thickness of the synthesised $MAPbBr_3$ NPLs.

3.2. X-ray diffraction and scattering analysis

For the XRD investigation, the sample was prepared by casting 50× 10.0 μL drops of the colloidal dispersion onto the flat side of a cleaned low-scattering sample holder, and the toluene solvent was allowed to evaporate between each drop cast; the sample holder with the deposited NPLs was then stored in the dark at 2–3 °C overnight before measurement. Software package MicroStructure (MStruct),[35–37] which implements the whole powder pattern modelling (WPPM) method[38] alongside the FOX/ObjCryst program,[39,40] was used to analyse the XRD pattern of the deposited sample. Peak intensities were calculated from a known crystal structure, obtained from the powder diffraction file (PDF-5+) no. 00-069-1345; peak positions and their shifts were determined by refining unit-cell parameters and accounting for the refraction at the sample interface. Peak broadening was modelled using numerical convolution of a known pseudo-Voigt instrumental broadening function, assuming that the crystallite sizes follow a log–normal distribution, and several other refinable parameters. Fig. 2 shows the measured XRD pattern and the MStruct fitting result of the synthesised $MAPbBr_3$ NPLs.

The XRD pattern of the synthesised $MAPbBr_3$ NPLs revealed a cubic-perovskite phase with space group $Pm\bar{3}m$, matching well with the PDF-5+ 00-069-1345, demonstrating that the synthesised $MAPbBr_3$ NPLs were indeed in the $APbX_3$ stoichiometry. Characteristic peaks were evident at diffraction angles of 14.9° and 30.1°, corresponding to reflections from the (100)

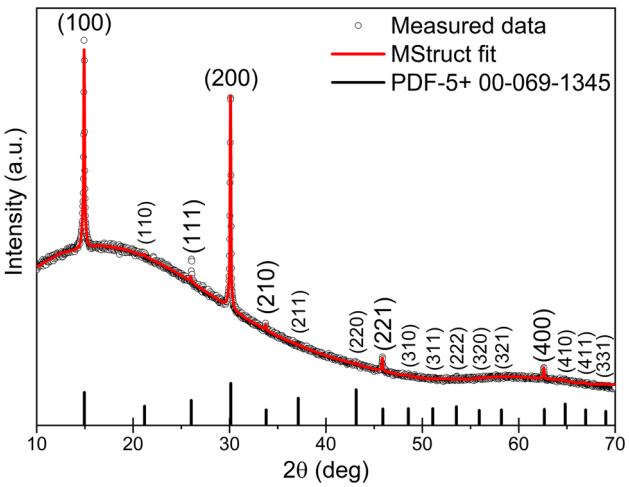

Fig. 2 XRD plot of the synthesised $MAPbBr_3$ NPLs.

and (200) planes, respectively; the diffraction angles are very slightly shifted to lower 2θ values as compared to the PDF. The deposited NPLs show a strong preference for alignment in the direction of the (100) plane, which follows the tendency of 2D perovskites to thermodynamically favour the 'face-on' orientation, where the surface normal vector aligns in a direction perpendicular to the substrate plane.[32] However, such strong orientation of the deposited sample was only observed after overnight cooling, without which the XRD pattern of the synthesised NPLs exhibited a more randomly oriented polycrystalline behaviour. The overnight cooling of the large amount of the deposited sample promoted the self-assembly of the drop cast NPLs into a structure more akin to a thin-film as it transitioned from a dispersion to a fully-crystalline multi-layer solid state,[3,5,32] which it was then observed to maintain for at least 24 hours in ambient atmosphere and room temperature even under exposure to a X-ray beam. This is further supported by the fact that the best possible fit was obtained by modelling the pattern on the basis of two simultaneously occurring cubic perovskite phases with the same space group and crystal struc-

ture, but different NPL sizes. The smaller phase exhibited a crystallite size = 18.36 ± 0.22 nm and a cubic lattice parameter a = 5.93923 ± 0.00031 Å, which is in good agreement with the NPL size obtained from the STEM analysis, while the larger phase exhibited a crystallite size = 117.93 ± 2.89 nm and a cubic lattice parameter a = 5.93102 ± 0.00021 Å.

For the SAXS investigation, the sample was prepared by injecting the colloidal dispersion into a borosilicate glass capillary with diameter of 1.5 mm and sealed with UV-hardening glue. The SAXS images obtained from the measurement of the samples and the buffer (pure toluene prepared similarly) were azimuthally integrated to obtain 1D SAXS curves. The buffer signal was then subtracted from the sample signal, and the resulting 1D SAXS curve was fitted using SasView v6.0.1. Initially, the SAXS curve was fitted with a Guinier–Porod function, which calculates the scattering for a generalised power law object.[41] The function is of the form,

$$I(Q) = \begin{cases} \dfrac{G}{Q^{s}} \exp\left[\dfrac{-Q^2 {R_g}^2}{3-s}\right] & Q \le Q_1 (\text{Guinier form}) \\ \dfrac{D}{Q^{m}} & Q \ge Q_1 (\text{Porod form}) \end{cases}$$

where $I(Q)$ is the scattered intensity, Q is the scattering variable, G is the Guinier scale factor, D is the Porod scale factor, and m is the Porod exponent. The value of Q_1 is not set but calculated internally maintaining the requirement of continuous values for the Guinier and Porod terms and their derivatives (slopes) at Q_1. Fig. S1 in the SI shows the SAXS curve fitted with the Guinier–Porod function; optimisation of the function outputted a radius of gyration R_g = 6.822 ± 0.012 nm and a dimension variable s = 1.98. The dimension variable reveals that the shape of the $MAPbBr_3$ NPLs, as observed in the colloidal dispersion, is very close to that of a platelet (s = 2). From this observation, different models in the SasView software, namely the cylinder, the parallelepiped, the lamellar and the sphere models, were also used to fit the measured SAXS data. The best fit was obtained from using the lamellar model for dilute, lyotropic, randomly oriented, 'infinitely large' sheets with polydispersity in the lamellae thickness.[42,43] The scattering intensity $I(q)$ is given as,

$$I(q) = \frac{2\pi P(q)}{q^2 \delta}$$

and the form factor $P(q)$ is given as,

$$P(q) = \frac{2\Delta\rho^2}{q^2}(1 - \cos(q\delta)) = \frac{4\Delta\rho^2}{q^2}\sin^2\left(\frac{q\delta}{2}\right)$$

where $\Delta\rho$ is the scattering length density difference, and δ is the total layer thickness. Fig. 3 shows the SAXS curve fitted with the lamellar model. The scattering length density of the solvent (toluene) was fixed, and the optimisation of the other parameters yielded a thickness = 13.536 ± 0.097 nm and a polydispersity ratio (Gaussian distribution of thickness) = 1. The R_g and the NPL thickness obtained from the SAXS analysis are smaller than the NPL sizes obtained from the STEM and the XRD analyses. This is to be expected, because the sample

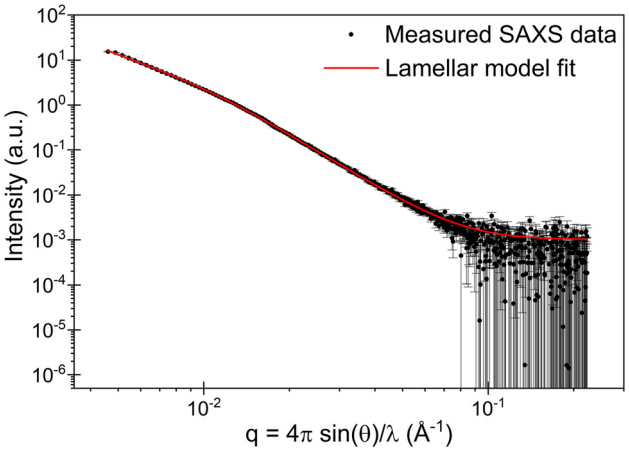

Fig. 3 SAXS plot and Lamellar model fit of the colloidal dispersion of the synthesised $MAPbBr_3$ NPLs.

investigated in the SAXS analysis is a relatively low concentration dispersion, while the sample investigated in the XRD analysis is deposited in large amounts and develops a crystalline solid-state character like a thin-film with overnight cooling. The discrepancy between the sizes obtained from the STEM and SAXS analyses occurs because of the destructive effect of the high-energy STEM electron beam on the synthesised $MAPbBr_3$ NPLs, which would have rapidly melted the smallest NPLs in the process of an acquisition, thereby skewing the size-distribution towards slightly larger NPLs.

3.3. Ensemble optical analysis

To investigate the ensemble optical properties, the samples were prepared by transferring 3 mL of the colloidal dispersion in a clean quartz cuvette. The UV-visible absorption spectrum was measured in the range of 320–800 nm with the pure toluene solvent as a reference, while the ensemble PL spectrum was measured in the range of 410–688 nm with an excitation wavelength of 405 nm; Fig. 4(a) shows the measured ensemble optical spectra of the synthesised $MAPbBr_3$ NPLs. The synthesised NPLs exhibited a broad absorption onset in the visible region with a pronounced shoulder at ~510 nm, and a sharp PL emission peak centred at 518 nm (corresponding to a bright green colour) with a FWHM of 26 nm and a lightly asymmetric tail towards longer wavelengths; the small Stokes shift is evident of the direct exciton recombination as the primary originator of the PL.

The obtained ensemble optical properties exhibit a strong blue-shift when compared to previously published reports of $MAPbBr_3$ single crystals and thin-films,[44–46] but are closely matching to previously published reports of $MAPbBr_3$ NPLs. The blue-shift is understood as a consequence of the quantum size confinement of the NPLs in terms of their thickness, which structurally consists of multiple single perovskite layers of corner-sharing $PbBr_6^{2-}$ octahedral sheets, intercalated with methylammonium cations and stabilised by longer alkyl chain ligands. Typically, the bright-green emission exhibited by our

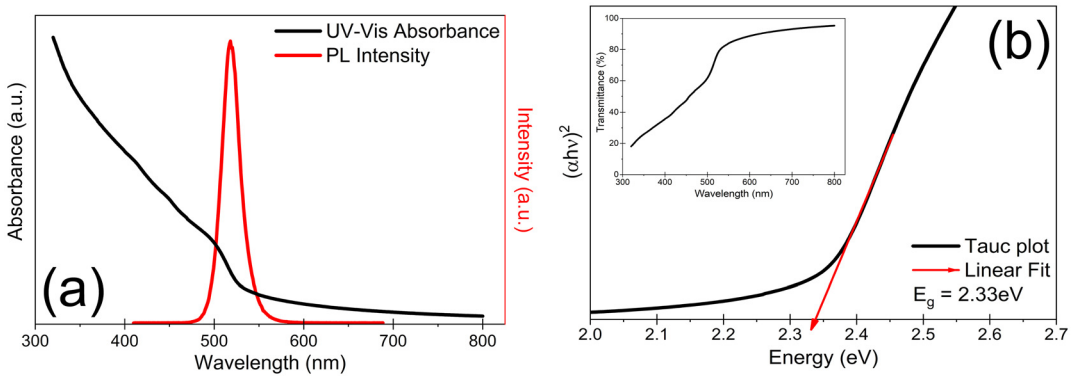

Fig. 4 (a) Ensemble optical absorption and emission spectra of the colloidal dispersion of synthesised $MAPbBr_3$ NPLs; (b) Tauc plot obtained from the ensemble UV-visible absorption spectroscopy of the colloidal dispersion of synthesised $MAPbBr_3$ NPLs. Inset shows the transmittance obtained from the UV-visible absorption spectroscopy.

synthesised $MAPbBr_3$ NPLs is characteristic of 5–7 $PbBr_6^{2-}$ layers, placing the colloidal ensemble in a weak confinement regime when compared to the Bohr excitonic radius of $MAPbBr_3$ (~2 nm).[30,32–34] $MAPbBr_3$ NPLs consisting of 5–7 $PbBr_6^{2-}$ layers exhibit a thickness of ~3–6 nm, accounting for the size of a $MAPbBr_3$ monolayer (~0.6 nm) and a ligand length of ~1.5 nm.[30,32,33] The discrepancy with the thickness obtained from the SAXS analysis of the ensemble dispersion can be attributed to the gradual formation of stacked NPLs separated by intercalating long-chain alkyl ligands; the extended measurement time leads to limited self-assembly in the undisturbed dispersion under prolonged exposure to the X-ray beam. However, the confined thickness of the synthesised NPLs is in agreement with the height distribution obtained from the AFM analysis performed in the upcoming section. The strong absorption of the synthesised LHPs at wavelengths longer than the absorption onset is characteristic of a direct band-gap semiconductor, and Tauc-plot analysis has been employed to obtain the energy band-gap E_g = 2.3 eV of the synthesised $MAPbBr_3$ NPLs, which is in good agreement with previously published reports on $MAPbBr_3$ semiconductor thin-films.[47–49] Fig. 4(b) shows the Tauc plot obtained from the UV-visible absorption spectroscopy of the synthesised $MAPbBr_3$ NPLs, and the inset in the same shows the optical transmission spectra, which highlights the nearly transparent nature of the film at wavelengths longer than the absorption onset.

The PLQY was calculated to be ~50(±5)%, which is quite an improvement on the QY obtained from $MAPbBr_3$ thin-films and bulk materials, and is comparable to previously published reports of $MAPbBr_3$ quantum dots and NPLs.[50–52] The improvement of QY in the colloidal $MAPbBr_3$ NPLs as compared to thin-film or bulk structures even at low excitation densities is a result of the significant increase in the Wannier type exciton binding energy, which inhibits the dissociation of the exciton before radiative decay, and also as a result of the quenching of radiative losses (which are caused by the reabsorption of emitted photons) because of the low concentration of the colloidal dispersion. Fig. S2 in the SI shows the time-resolved ensemble PL decay curve of the synthesised $MAPbBr_3$ NPLs, fitted with a single-exponential decay function, yielding a PL decay time τ_{PL} = 11.9 ns, considerably extended as compared to $MAPbBr_3$ thin-films and single crystals. This single-exponential decay also supports the dominant radiative exciton decay as interpreted from the high PLQY.[30,50–52]

3.4. Single-dot spectroscopy

For single particle spectroscopic investigation, the sample was prepared by casting 1 μL of the colloidal dispersion onto a rigorously cleaned and dried silica wafer, followed by spin coating at 6000 rpm for 1 minute; the spin coating formed a coffee-ring structure of the deposited $MAPbBr_3$ NPLs. Fig. S3 in the SI shows SEM images of the spin-coated sample wafer, which exhibit the well-isolated single $MAPbBr_3$ NPLs. The spectra of the individual NPLs were analysed and extracted using WinSpec/32 v2.5.12.2 software. Fig. 5(a) shows a typical spectral image of the sample on the camera; the vertical red box highlights the image of the slit, and the horizontal red box highlights the emission spectra of a single NPL. Fig. 5(b) shows the emission spectrum integrated over 3 lines for a single NPL marked in Fig. 5(a) with a horizontal red box. Most NPLs exhibited a multi-peak emission, and Gaussian fitting was employed to deconvolute the peaks and obtain their peak centres where necessary. 481 individual NPLs were analysed by binning the wavelength of the emission peak maxima with a binning size of 10 nm; Fig. 6 shows this emission peak maxima binning histogram. Fig. S4–S7 in the SI show a similar illustration of spectral images of the sample followed by the emission spectrum of an individual NPL – however, these images highlight the emission spectra differentiated by the number of emission peaks exhibited. Individual histograms were constructed to illustrate the binning of peak centres with respect to the number of emission peaks exhibited and can be seen in the SI Fig. S4–S7 and S8.

The most obvious observable difference between the spectra of the individual NPLs and the ensemble luminescence

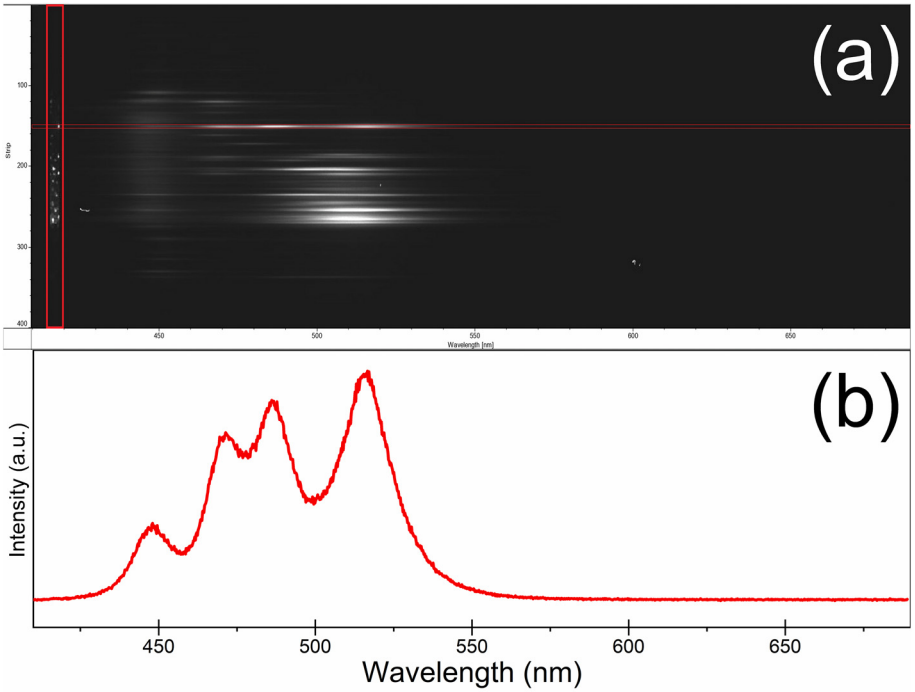

Fig. 5 (a) Typical spectral image of the sample captured on the camera in a SDS measurement, the vertical red box highlights the image of the slit, and the horizontal red box highlights the emission spectrum of a single $MAPbBr_3$ NPL; (b) emission spectrum integrated over 3 lines for a single $MAPbBr_3$ NPL marked in (a) with a horizontal red box.

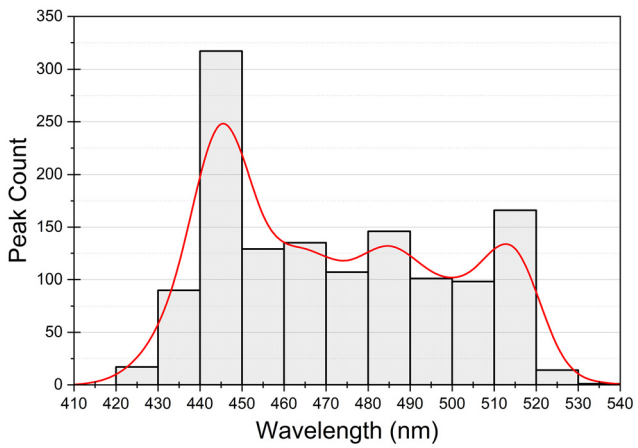

Fig. 6 Frequency count histogram depicting the wavelength binning of the emission peak maxima obtained from the extracted emission spectrum of single nanoplatelets.

spectrum of the $MAPbBr_3$ colloidal dispersion is the multi-peak emission of the individual NPLs; such a multi-peak emission (not caused by the presence of $PbBr_2$ defects or impurity) has been observed for $MAPbBr_3$ NPLs and NPs before.[33,34,53] However, to the best of the knowledge of the authors, such multi-peak emission has never been reported in the literature for single isolated square-shaped $MAPbBr_3$ NPLs synthesised using a non-template ligand-assisted reprecipitation route. The most frequently observed peak centres were at wavelength values of ~445 nm (2.78 eV), ~465 nm (2.67 eV), ~485 nm (2.55 eV) and ~515 nm (2.40 eV), with the highest frequency of emission peaks at ~445 nm (Fig. 6). Interestingly, individual $MAPbBr_3$ NPLs that exhibited an emission peak centred around 515 nm also exhibited emission peaks at the other wavelengths; however, the converse was rarely true, *i.e.*, there were a greater number of individual NPL emissions that only exhibited one or two peaks at shorter wavelengths and did not exhibit an emission peak around 515 nm (SI Fig. S4–S7). This can be explained by the quantum confinement of $MAPbBr_3$ NPLs depending on their thickness, or the number of $PbBr_6^{2-}$ layers in the NPL structure. The modified energy band-gap structure of 2D semiconductors is analogous to a theoretical quantum well. In the case of our synthesised $MAPbBr_3$ NPLs, the energy band-gap structure can be understood as a 2-step quantum well, with the core 2D $MAPbBr_3$ being surrounded by long-chain alkyl ligands with strong (but not infinite) confinement energy. As has been noted above, the bright green emission exhibited by the ensemble dispersion of our synthesised $MAPbBr_3$ NPLs is characteristic of 5–7 $PbBr_6^{2-}$ layers. Similarly, by comparing the emission peak centres with previously reported values of PL emission peaks attributed to specific number of $PbBr_6^{2-}$ layers, the emission peaks centred at wavelengths of ~445 nm, ~465 nm, and ~485 nm can be attributed to 2, 3 and 4 $PbBr_6^{2-}$ layers, respectively.[32–34,53]

The reason why these multi-peak emissions are not exhibited in the PL of the colloidal dispersion of our synthesised $MAPbBr_3$ NPLs could be multi-fold. The simplest of the reasons is that the emission from the thinner layers of the

NPLs is simply reabsorbed by the main emitting species in the colloidal dispersion; however, this is less likely due to reasons already mentioned in the discussion above of the enhanced PLQY exhibited by the ensemble dispersion of the synthesised $MAPbBr_3$ NPLs. The more likely reason is the existence of surface trap states that quench the emission from thinner NPL layers, which is a phenomenon that is quite well documented in the case of semiconductor nanoparticles, owing to the increasing surface-to-volume ratio with decreasing size.[54–56] To prepare the samples for SDS, the thin $MAPbBr_3$ NPLs were spin-coated onto a substrate, which exposed them to the oxygen in the atmosphere. Oxygen molecules have been reported to play an important role in the PL activation of $MAPbBr_3$ NPs and thin-films, by quenching trapping sites by surface reaction or the formation of superoxide species.[24,26,57] Similarly, the presence of oxygen from the gas phase promoted photooxidation and inhibited Auger recombination in the deposited $MAPbBr_3$ NPLs, allowing for the observable emission peaks attributed to the thinner layers.[24,26,57]

Another mechanism that has been reported for the emission enhancement in $MAPbBr_3$ NPLs is laser-assisted photoactivation, in which photooxidation promoted by atmospheric oxidation is further facilitated by the continuous generation of photoinduced charges which contribute to the passivation of surface defects, leading to an improved PL response.[24,26,54,57] The lack of any significant changes observed in the shape and position of the individual emission peaks, only in the number of peaks and their relative intensity, further suggests the role of this mechanism in the present work. In a typical SDS measurement, the sample spin-coated onto a cleaned silica wafer was excited by a continuous laser, and once a spectral image was captured by the camera, the sample wafer was moved slightly to obtain the spectral image of a new population on the wafer, all while the sample was continuously irradiated by the laser. In this manner, 4–5 spectral images were obtained from each sample wafer before the NPLs started exhibiting PL deactivation, after which the sample wafer was replaced by a new silica wafer freshly spin-coated with the sample NPLs. The PL deactivation probably occurred due to the irreversible degradation of the perovskite structure by continuous laser irradiation, or possibly due to the prolonged air-exposure of the NPLs initially covered with a toluene droplet (as can be seen in the proceeding AFM analysis). Fig. S9 in the SI shows the emission spectra integrated over the wafer area under the slit across 4 successive spectral image captures, *i.e.*, Fig. S9 shows the emission spectra from 4 different populations of NPLs that have been continuously laser irradiated for increasing time from the 1^{st} to the 4^{th} capture. From Fig. S9 it can be inferred that the continuous irradiation of the sample not only significantly increases the PL intensity, but also gradually leads to the emission of more prominent peaks centred at longer wavelengths, which supports the role of the laser-assisted photoactivation mechanism in the present work.[24,26,54,57]

To further support the viability of this mechanism, AFM images of the samples were obtained, as shown in Fig. S10 in the SI. The first image (Fig. S10(a)) was obtained 2 hours after the sample was cast onto mica, and the second image (Fig. S10(c)) was obtained 48 hours later. From the AFM images it can be observed that the deposited NPLs are initially surrounded by toluene even after the bulk of the solvent has evaporated. After 48 hours in ambient conditions, the toluene appears to have completed evaporated from the edges of the deposited NPLs but is still present in nano-sized globules on the surface of the NPL core. This can be considered equivalent to the sample state when it was first exposed to the continuous laser excitation after spin coating. The continuous laser irradiation helped evaporate the nanoscale toluene and expose more of the NPL to the atmospheric oxygen, starting with the thinner edges first, a morphological feature of the synthesised NPLs that can also be observed in the SEM image shown in Fig. S3; this leads to the initial observation of higher intensity emission peaks centred at shorter wavelengths (Fig. S9, 1^{st} capture). As more of the toluene is evaporated with the continuous laser exposure of the sample, more of the thicker NPL core (again, morphologically observable in SEM Fig. S3) is exposed to the atmospheric oxygen, which gradually leads to the observation of higher intensity emission peaks centred at longer wavelengths (Fig. S9, 4^{th} capture). This state can be considered equivalent to the AFM image obtained 430 hours after the sample was initially cast onto mica (Fig. S10(e)); the size distribution histogram obtained from the same (Fig. S10(f)) is similar to that obtained from the STEM analysis, since the incident high energy electron beam and the effect of the vacuum chamber would have evaporated all the nanoscale toluene present on the sample cast onto the TEM grid.

4. Conclusions

We have developed a modified ligand-assisted reprecipitation synthesis protocol for $MAPbBr_3$ NPLs that employs concepts from reverse microemulsion methods to enhance phase purity, morphology control, and colloidal stability. The resulting NPLs exhibit ultra-thin square morphology with lateral dimensions of 17–20 nm as confirmed by STEM imaging. XRD patterns show strong (100) reflection characteristic of the cubic perovskite phase ($Pm\bar{3}m$), and MStruct fitting reveals the contribution from two crystallite sizes of 18.3 nm and 117.9 nm. Small-angle X-ray scattering (SAXS) data fitted using a Guinier–Porod function reveals a dimension variable indicating quasi-2D confinement and corroborating the morphology obtained from STEM analysis, and when fitted using a lamellar model yields a thickness of 13.5 nm. Tauc plot analysis of the optical absorption spectrum indicates a direct band-gap of 2.3 eV, reflecting the effects of quantum confinement. Steady-state photoluminescence spectra display a narrow emission centred at 518 nm (FWHM = 26 nm), with a quantum yield of ~50% and a single-exponential PL decay time τ_{PL} of 11.9 ns. SDS reveals multiple emission peaks per NPL, suggesting energy quantization arising from strong lateral confinement and dielectric contrast at the ligand–NPL interface. The SDS analysis confirms the contribution of the atmospheric oxygen in

the observation and enhancement of multi-peak PL emission, and the contribution of continuous irradiation by an excitation laser in the observation and enhancement of emission peaks at longer wavelengths. These observations underscore the role of both quantum and dielectric confinement in modulating the excitonic landscape of $MAPbBr_3$ NPLs. Altogether, our approach yields structurally coherent, quantum-confined $MAPbBr_3$ NPLs, that are stable for at least 4 months in a dispersion, with bright, size-tuneable emission and narrow linewidths – key requirements for next-generation optoelectronic devices such as perovskite-based LEDs, single-photon sources, and ultrathin photodetectors. The synthetic strategy and in-depth structure–property correlations presented herein provide a versatile platform for advancing the fundamental understanding and application of 2D hybrid organic–inorganic lead-based halide perovskites.

Author contributions

Suhaas Gupta: conceptualisation, data curation, formal analysis, funding acquisition, investigation, methodology, resources, software, visualisation, writing – original draft; Dmytro Vorontsov: data curation (ensemble optical analysis, SDS), investigation (ensemble optical analysis, SDS), writing – review and editing; Anna Fučíková: data curation (SDS, AFM), formal analysis (SDS, AFM), investigation (SDS, AFM), methodology (SDS, AFM), resources (SDS, AFM), supervision (SDS, AFM), visualisation (SDS, AFM), writing – review and editing; František Trojánek: data curation (PL decay), investigation (PL decay), resources (PL decay); Dominika Zákutná: methodology (synthesis), resources (synthesis), supervision (synthesis), writing – review and editing; Jozef Veselý: data curation (STEM), investigation (STEM), resources (STEM); Petr Harcuba: data curation (SEM), investigation (SEM), resources (SEM); Milan Dopita: data curation (XRD, SAXS), formal analysis (XRD, SAXS), funding acquisition, investigation (XRD, SAXS), methodology (XRD, SAXS), resources (XRD, SAXS), software (XRD, SAXS) supervision (XRD, SAXS), visualisation (XRD, SAXS), writing – review and editing.

Conflicts of interest

The authors declare that they have no known conflicting financial interests or personal relationships that could have appeared to influence the work reported in this paper.

Data availability

All the data generated or analysed during this study has been deposited in this manuscript and in the SI. All the compared data was properly cited and included in the reference section following the journal style. The data will be made available from the corresponding author on reasonable request.

Supplementary information (SI) is available. See DOI: https://doi.org/10.1039/d5nr04000k.

Acknowledgements

Suhaas Gupta acknowledges the funding received from the Charles University Grant Agency (GAUK project no. 206423). Milan Dopita and Suhaas Gupta acknowledge the financial support of the Czech Science Foundation (GACR project no. 23-06543S). This work benefited from the use of the SasView application, originally developed under NSF Award DMR-0520547. SasView also contains code developed with funding from the EU Horizon 2020 programme under the SINE2020 project Grant No. 65400.

References

1 A. G. Belous, A. A. Ishchenko, O. I. V'yunov and P. V. Torchyniuk, Preparation and properties of films of organic-inorganic perovskites $MAPbX_3$ (MA = CH_3NH_3; X = Cl, Br, I) for solar cells: a review, *Theor. Exp. Chem.*, 2021, **56**(6), 359–386.

2 Z. Gan, Y. Cheng, W. Chen, K. P. Loh, B. Jia and X. Wen, Photophysics of 2D organic–inorganic hybrid lead halide perovskites: progress, debates, and challenges, *Adv. Sci.*, 2021, **8**(6), 2001843.

3 L. Ke, S. Luo, X. Ren and Y. Yuan, Factors influencing the nucleation and crystal growth of solution-processed organic lead halide perovskites: a review, *J. Phys. D: Appl. Phys.*, 2021, **54**(16), 163001.

4 Y. Tong, A. Najar, L. Wang, L. Liu, M. Du, J. Yang, J. Li, K. Wang and S. Liu, Wide–bandgap organic–inorganic lead halide perovskite solar cells, *Adv. Sci.*, 2022, **9**(14), 2105085.

5 J. Di, J. Chang and S. Liu, Recent progress of two–dimensional lead halide perovskite single crystals: crystal growth, physical properties, and device applications, *EcoMat*, 2020, **2**(3), e12036.

6 H. B. Lee, N. Kumar, B. Tyagi, S. He, R. Sahani and J. W. Kang, Bulky organic cations engineered lead-halide perovskites: a review on dimensionality and optoelectronic applications, *Mater. Today Energy*, 2021, **21**, 100759.

7 M. J. Islam, K. Pal, M. Harun-Ur-Rashid, A. Kumar, M. F. Hossain, N. Asthana, S. Rajendran, S. Vallinayagam and A. Malik, Optical maneuvering of photofunctioning hybrid perovskite for future photonics potential application, *J. Mol. Liq.*, 2024, **408**, 125343.

8 X. Dong, Y. Shen, F. Wang, Z. He, Y. Zhao, Z. Miao and Z. Wu, $MAPbX_3$ perovskite single crystals for advanced optoelectronic applications: progress, challenges, and perspective, *Small*, 2025, **21**(11), 2412809.

9 C. Lin, Stabilizing organic–inorganic lead halide perovskite solar cells with efficiency beyond 20%, *Front. Chem.*, 2020, **8**, 592.

10 E. C. Mahen, F. A. Permatasari, O. Floweri, B. W. Nuryadin, M. A. Irham, S. Z. Bisri, A. H. Aimon and F. Iskandar, Evolutions of the optical properties in green-emitting $MAPbBr_3$ perovskite nanoplatelets/polymethyl methacrylate

(PMMA) composite films for light-emitting diode applications, *J. Lumin.*, 2022, **248**, 118954.
11 X. Zhan, Progress on perovskite quantum dots and light-emitting diodes, *Appl. Comput. Eng.*, 2024, **98**, 125–132.
12 R. X. Chen, X. Q. Su, J. Wang, D. W. Gao, Y. Pan, Y. M. Wang and L. Wang, The roles of surface defects in $MAPbBr_3$ and multi-structures in $MAPbI_3$, *Opt. Mater.*, 2021, **122**, 111600.
13 S. Parveen, M. Das, S. Ghosh and P. K. Giri, Experimental and theoretical study of europium-doped organometal halide perovskite nanoplatelets for UV photodetection with high responsivity and fast response, *Nanoscale*, 2022, **14**(17), 6402–6416.
14 S. Pervaiz, M. Aamir, Q. Wali, M. E. Khan, M. Sattar and M. Sher, Fabrication of aqueous stable $CH_3NH_3PbBr_3$ perovskite: Addressing optoelectronics and fluorescent sensing applications, *Sustainable Chem. Environ.*, 2024, **5**, 100059.
15 C. Jin, M. Feng, J. Zhong, X. Sun, J. Wu, Q. Li, J. Gu and S. Liu, Insights into mechanism of size-controlled synthesis of $CH_3NH_3PbBr_3$ perovskite quantum dots and large nanoparticles with tunable optical properties, *Org. Electron.*, 2020, **82**, 105712.
16 A. Feng, X. Jiang, X. Zhang, X. Zheng, W. Zheng, O. F. Mohammed, Z. Chen and O. M. Bakr, Shape control of metal halide perovskite single crystals: from bulk to nanoscale, *Chem. Mater.*, 2020, **32**(18), 7602–7617.
17 H. E. Masitoh, F. A. Permatasari, B. W. Nuryadin, A. H. Aimon and F. Iskandar, Photoluminescence stability of $CH_3NH_3PbBr_3$ perovskite nanoparticles by adding SiO_2: Preliminary study, *Mater. Today: Proc.*, 2021, **44**, 3309–3312.
18 K. Hills-Kimball, H. Yang, T. Cai, J. Wang and O. Chen, Recent advances in ligand design and engineering in lead halide perovskite nanocrystals, *Adv. Sci.*, 2021, **8**(12), 2100214.
19 H. Shankar, S. Ghosh and P. Kar, Boosting the stability of lead halide perovskite nanocrystals by metal–organic frameworks and their applications, *J. Mater. Chem. C*, 2022, **10**(32), 11532–11554.
20 Z. Zhuang, J. Wang, J. Huang, R. Hong, C. Tao, Q. Wang, H. Lin, Z. Han, D. Zhang and S. Zhuang, Fabrication of High-Stability and-Sensitivity Perovskite Nanoparticles with a Core–Shell Structure for Surface-Enhanced Raman Scattering, *J. Phys. Chem. C*, 2024, **128**(24), 10120–10132.
21 C. P. Byers, B. S. Hoener, W. S. Chang, M. Yorulmaz, S. Link and C. F. Landes, Single-particle spectroscopy reveals heterogeneity in electrochemical tuning of the localized surface plasmon, *J. Phys. Chem. B*, 2014, **118**(49), 14047–14055.
22 J. Zhou, A. I. Chizhik, S. Chu and D. Jin, Single-particle spectroscopy for functional nanomaterials, *Nature*, 2020, **579**(7797), 41–50.
23 A. Al-Zubeidi, L. A. McCarthy, A. Rafiei-Miandashti, T. S. Heiderscheit and S. Link, Single-particle scattering spectroscopy: fundamentals and applications, *Nanophotonics*, 2021, **10**(6), 1621–1655.
24 T. Tachikawa, I. Karimata and Y. Kobori, Surface charge trapping in organolead halide perovskites explored by single-particle photoluminescence imaging, *J. Phys. Chem. Lett.*, 2015, **6**(16), 3195–3201.
25 D. J. Freppon, L. Men, S. J. Burkhow, J. W. Petrich, J. Vela and E. A. Smith, Photophysical properties of wavelength-tunable methylammonium lead halide perovskite nanocrystals, *J. Mater. Chem. C*, 2017, **5**(1), 118–126.
26 Y. Kimura, I. Karimata, Y. Kobori and T. Tachikawa, Mechanistic Insights into Photochemical Reactions on $CH_3NH_3PbBr_3$ Perovskite Nanoparticles from Single–Particle Photoluminescence Spectroscopy, *ChemNanoMat*, 2019, **5**(3), 340–345.
27 A. Jana and K. S. Kim, Effect of organic–cation exchange reaction of perovskites in water: H-bond assisted self-assembly, black phase stabilization, and single-particle imaging, *ACS Appl. Energy Mater.*, 2019, **2**(6), 4496–4503.
28 I. Karimata and T. Tachikawa, In Situ Exploration of the Structural Transition during Morphology–and Efficiency–Conserving Halide Exchange on a Single Perovskite Nanocrystal, *Angew. Chem.*, 2021, **133**(5), 2578–2583.
29 F. Zhang, H. Zhong, C. Chen, X. G. Wu, X. Hu, H. Huang, J. Han, B. Zou and Y. Dong, Brightly luminescent and color-tunable colloidal $CH_3NH_3PbX_3$ (X = Br, I, Cl) quantum dots: potential alternatives for display technology, *ACS Nano*, 2015, **9**(4), 4533–4542.
30 I. Rosa-Pardo, R. B. Cevallos-Toledo, L. Polavarapu, R. Arenal, R. E. Galian and J. Perez-Prieto, Revisiting the nontemplate approach for the synthesis of highly green emissive hybrid perovskite nanocrystals: platelets or spheres?, *Nanoscale*, 2022, **14**(4), 1160–1164.
31 F. Zhu, L. Men, Y. Guo, Q. Zhu, U. Bhattacharjee, P. M. Goodwin, J. W. Petrich, E. A. Smith and J. Vela, Shape evolution and single particle luminescence of organometal halide perovskite nanocrystals, *ACS Nano*, 2015, **9**(3), 2948–2959.
32 S. Kumar, J. Jagielski, S. Yakunin, P. Rice, Y. C. Chiu, M. Wang, G. Nedelcu, Y. Kim, S. Lin, E. J. Santos and M. V. Kovalenko, Efficient blue electroluminescence using quantum-confined two-dimensional perovskites, *ACS Nano*, 2016, **10**(10), 9720–9729.
33 Y. Tong, F. Ehrat, W. Vanderlinden, C. Cardenas-Daw, J. K. Stolarczyk, L. Polavarapu and A. S. Urban, Dilution-induced formation of hybrid perovskite nanoplatelets, *ACS Nano*, 2016, **10**(12), 10936–10944.
34 J. A. Sichert, Y. Tong, N. Mutz, M. Vollmer, S. Fischer, K. Z. Milowska, R. García Cortadella, B. Nickel, C. Cardenas-Daw, J. K. Stolarczyk and A. S. Urban, Quantum size effect in organometal halide perovskite nanoplatelets, *Nano Lett.*, 2015, **15**(10), 6521–6527.
35 Z. Matěj, R. Kužel and L. Nichtová, XRD total pattern fitting applied to study of microstructure of TiO_2 films, *Powder Diffr.*, 2010, **25**(2), 125–131.
36 Z. Matěj, A. Kadlecová, M. Janeček, L. Matějová, M. Dopita and R. Kužel, Refining bimodal microstructure of materials with MSTRUCT, *Powder Diffr.*, 2014, **29**(S2), S35–S41.

37 MStruct-software for Micro Structure analysis by powder diffraction (xray.cz/mstruct).
38 P. Scardi and M. Leoni, Whole powder pattern modelling, *Acta Crystallogr. A*, 2002, **58**(2), 190–200.
39 V. Favre-Nicolin and R. Černý, FOX,free objects for crystallography': a modular approach to ab initio structure determination from powder diffraction, *Appl. Crystallogr.*, 2002, **35**(6), 734–743.
40 FoxWiki-FOX, Free Objects for Crystallography Wiki (fox.vincefn.net).
41 B. Hammouda, A new Guinier–Porod model, *Appl. Crystallogr.*, 2010, **43**(4), 716–719.
42 F. Nallet, R. Laversanne and D. Roux, Modelling X-ray or neutron scattering spectra of lyotropic lamellar phases: interplay between form and structure factors, *J. Phys. II*, 1993, **3**(4), 487–502.
43 J. Berghausen, J. Zipfel, P. Lindner and W. Richtering, Influence of water-soluble polymers on the shear-induced structure formation in lyotropic lamellar phases, *J. Phys. Chem. B*, 2001, **105**(45), 11081–11088.
44 B. Wenger, P. K. Nayak, X. Wen, S. V. Kesava, N. K. Noel and H. J. Snaith, Consolidation of the optoelectronic properties of $CH_3NH_3PbBr_3$ perovskite single crystals, *Nat. Commun.*, 2017, **8**(1), 590.
45 H. Ji, Z. Shi, X. Sun, Y. Li, S. Li, L. Lei, D. Wu, T. Xu, X. Li and G. Du, Vapor-assisted solution approach for high-quality perovskite $CH_3NH_3PbBr_3$ thin films for high-performance green light-emitting diode applications, *ACS Appl. Mater. Interfaces*, 2017, **9**(49), 42893–42904.
46 G. Weng, J. Xue, J. Tian, X. Hu, X. Bao, H. Lin, S. Chen, Z. Zhu and J. Chu, Picosecond random lasing based on three-photon absorption in organometallic halide $CH_3NH_3PbBr_3$ perovskite thin films, *ACS Photonics*, 2018, **5**(7), 2951–2959.
47 J. Chaudhary, S. Choudhary, C. M. Negi, S. K. Gupta and A. S. Verma, Surface morphological, optical and electrical characterization of methylammonium lead bromide perovskite ($CH_3NH_3PbBr_3$) thin film, *Phys. Scr.*, 2019, **94**(10), 105821.
48 S. J. Chang, L. C. Li, T. H. Hong, M. Shellaiah and K. W. Sun, Fabrication of centimeter-scale $MAPbBr_3$ light-emitting device with high color purity, *Org. Electron.*, 2020, **86**, 105931.
49 J. N. Fru, N. Nombona and M. Diale, Synthesis and characterisation of methylammonium lead tri-bromide perovskites thin films by sequential physical vapor deposition, *Phys. B*, 2020, **578**, 411884.
50 S. Gonzalez-Carrero, R. E. Galian and J. Pérez-Prieto, Organic-inorganic and all-inorganic lead halide nanoparticles, *Opt. Express*, 2015, **24**(2), A285–A301.
51 S. Gonzalez-Carrero, R. E. Galian and J. Pérez-Prieto, Maximizing the emissive properties of $CH_3NH_3PbBr_3$ perovskite nanoparticles, *J. Mater. Chem. A*, 2015, **3**(17), 9187–9193.
52 Z. Yuan, Y. Shu, Y. Tian, Y. Xin and B. Ma, A facile one-pot synthesis of deep blue luminescent lead bromide perovskite microdisks, *Chem. Commun.*, 2015, **51**(91), 16385–16388.
53 S. Bhaumik, S. A. Veldhuis, Y. F. Ng, M. Li, S. K. Muduli, T. C. Sum, B. Damodaran, S. Mhaisalkar and N. Mathews, Highly stable, luminescent core–shell type methylammonium–octylammonium lead bromide layered perovskite nanoparticles, *Chem. Commun.*, 2016, **52**(44), 7118–7121.
54 K. Zheng, K. Zidek, M. Abdellah, M. E. Messing, M. J. Al-Marri and T. Pullerits, Trap states and their dynamics in organometal halide perovskite nanoparticles and bulk crystals, *J. Phys. Chem. C*, 2016, **120**(5), 3077–3084.
55 S. Gupta, R. K. Choubey, L. K. Sharma, M. P. Ghosh, M. Kar and S. Mukherjee, Exploring the magnetic ground state of vanadium doped zinc sulphide, *Semicond. Sci. Technol.*, 2019, **34**(10), 105006.
56 S. Gupta, A. Kumar, S. Mukherjee, K. K. Kushwah, S. K. Mahobia, P. Patharia, A. Kushwaha, D. Yadav, U. K. Dwivedi, S. Kumar and R. K. Choubey, Temperature-dependent study of the fabricated ZnS/p-Si heterojunction, *Phys. B*, 2023, **657**, 414831.
57 M. Anaya, J. F. Galisteo-López, M. E. Calvo, J. P. Espinós and H. Míguez, Origin of light-induced photophysical effects in organic metal halide perovskites in the presence of oxygen, *J. Phys. Chem. Lett.*, 2018, **9**(14), 3891–3896.